Effects of particle-fluid density ratio on the interactions between the turbulent channel flow and finite-size particles

Zhaosheng Yu,[1,*] Zhaowu Lin,[1] Xueming Shao,[1] and Lian-Ping Wang[2]

[1]*State Key Laboratory of Fluid Power and Mechatronic Systems, Department of Mechanics, Zhejiang University, Hangzhou 310027, China*

[2]*Department of Mechanical Engineering, University of Delaware, Newark, Delaware 19716, USA*

(Received 12 April 2017; revised manuscript received 20 July 2017; published 5 September 2017)

A parallel direct-forcing fictitious domain method is employed to perform fully resolved numerical simulations of turbulent channel flow laden with finite-size particles. The effects of the particle-fluid density ratio on the turbulence modulation in the channel flow are investigated at the friction Reynolds number of 180, the particle volume fraction of 0.84%, and the particle-fluid density ratio ranging from 1 to 104.2. The results show that the variation of the flow drag with the particle-fluid density ratio is not monotonic, with a larger flow drag for the density ratio of 10.42, compared to those of unity and 104.2. A significant drag reduction by the particles is observed for large particle-fluid density ratios during the transient stage, but not at the statistically stationary stage. The intensity of particle velocity fluctuations generally decreases with increasing particle inertia, except that the particle streamwise root-mean-square velocity and streamwise-transverse velocity correlation in the near-wall region are largest at the density ratio of the order of 10. The averaged momentum equations are derived with the spatial averaging theorem and are used to analyze the mechanisms for the effects of the particles on the flow drag. The results indicate that the drag-reduction effect due to the decrease in the fluid Reynolds shear stress is counteracted by the drag-enhancement effect due to the increase in the total particle stress or the interphase drag force for the large particle-inertia case. The sum of the total Reynolds stress and particle inner stress contributions to the flow drag is largest at the density ratio of the order of 10, which is the reason for the largest flow drag at this density ratio. The interphase drag force obtained from the averaged momentum equation (the balance theory) is significantly smaller than (but agrees qualitatively with) that from the empirical drag formula based on the phase-averaged slip velocity for large density ratios. For the neutrally buoyant case, the balance theory predicts a positive interphase force on the particles arising from the negative gradient of the particle inner stress, which cannot be predicted by the drag formula based on the phase-averaged slip velocity. In addition, our results show that both particle collision and particle-turbulence interaction play roles in the formation of the inhomogeneous distribution of the particles at the density ratio of the order of 10.

DOI: 10.1103/PhysRevE.96.033102

I. INTRODUCTION

Particle-laden turbulent flows are commonly encountered in natural and industrial settings, such as sediment transport, the paper industry, pipeline transport, and fluidized beds. It is important to understand the particle-turbulence interaction mechanisms in order to improve the macroscopic models for the multiphase flows and the design of the related device. The point-particle-approximation based direct numerical simulations have provided much insight into the particle-turbulence interactions; for example, such simulations showed that the particles could affect the fluid-phase turbulence even at small particle volume fractions (e.g., Squires and Eaton [1]; Ferrante and Elghobashi [2]; Vance *et al.* [3]), and the turbulence could significantly affect the motion and distribution of the particles (e.g., Wang and Maxey [4]). In principle, the point-particle model is suited to the case where the particle size is smaller than the turbulence Kolmogorov length scale. In recent years, the interface-resolved direct numerical simulation (DNS) methods have been developed to deal with the case where the particle size is comparable to or larger than the Kolmogorov length scale (Balachandar and Eaton [5]). The essential features of the interface-resolved methods are that the interfaces between the particles and the fluid are resolved and the hydrodynamic forces on the particles are determined from the solution of the flow fields outside the particle boundaries. Such methods have been applied to simulations of particle-laden isotropic homogeneous flows (e.g., Ten Cate *et al.* [6]; Lucci *et al.* [7]; Homann and Bec [8]; Gao *et al.* [9]; Cisse *et al.* [10]; Chouippe and Uhlmann [11]; Fornari *et al.* [12]; de Motta *et al.* [13]), pipe flow (Wu *et al.* [14]), vertical channel flows (Kajishima *et al.* [15]; Uhlmann 2008 [16]; García-Villalba *et al.* [17]), horizontal channel flows (e.g., Pan and Banerjee [18]; Shao *et al.* [19]; Kidanemariam *et al.* [20]; Do-Quang *et al.* [21]; Picano *et al.* [22]; Wang *et al.* [23]; Yu *et al.* [24,25]), as well as the interactions between the turbulence and a fixed particle (e.g., Bagchi and Balachandar [26]; Burton and Eaton [27]; Naso and Prosperetti [28]).

Regarding the interface-resolved DNS of the horizontal particle-laden channel flows, Shao *et al.* [19], Picano *et al.* [22], and Wang *et al.* [23] investigated the effects of the neutrally buoyant spherical particles on the turbulence, and observed that in the near-wall region the particles enhance the transverse and spanwise root-mean-square (RMS) velocity fluctuations, but reduce the maximum streamwise RMS velocity. In the center region, the particle effects are opposite to those in the near-wall region. In addition, the flow drag was found to be enhanced for the particle volume fraction of order 1% and 10% in all simulations. Loisel *et al.* [29] examined the effect of neutrally buoyant finite-size particles on the channel flow in the

*yuzhaosheng@zju.edu.cn

laminar-turbulent transition regime, and observed that particles increased the transverse RMS flow velocity fluctuations and broke down the flow coherent structures into smaller and sustained eddies, preventing the flow to relaminarize at the single-phase critical Reynolds number. Lashgari *et al.* [30] investigated numerically a channel flow laden with solid spherical particles for a wide range of Reynolds numbers, and identified three different regimes (laminar, turbulent, and inertial shear thickening) for different values of solid volume fraction and flow Reynolds number.

For most interface-resolved DNS of particle-laden channel flows in the literature, the particle-fluid density ratio was set according to the liquid-solid system, namely, of the order of unity, except in a very recent work of Fornari *et al.* [31] who studied the effect of the particle density in turbulent channel flow laden with finite-size particles in semidilute conditions with the particle-fluid density ratio up to 1000. Their results indicated that the flow drag was enhanced slightly as the density ratio was increased from unity to 10, and the effect was smaller than that of the particle volume fraction. The authors observed significant lateral migration of the particles toward the centerline of the channel at density ratios of the order of 10 due to the particle-inertia and shear flow effects. In addition, a preliminary work on the effects of the particle-fluid density ratio on the turbulent channel flow has been done in our recent work [32]. The aim of the present study is to report the significantly expanded results of the work [32]. Compared to [32], results such as the particle RMS (root-mean-square) velocities, the particle concentration distribution, and the interphase drag behavior are presented, and the effects of the density ratio on the flow drag are analyzed with the averaged momentum equation, which was derived by Picano *et al.* [22] using the phase indicator function for spatial averaging and is derived here with an alternative approach: the spatial averaging theorem. The main differences between the work of Fornari *et al.* [31] and our work are (1) the flow rate was fixed in their study, whereas the pressure gradient is fixed in our study; (2) regarding the parameter settings, the ratio of the particle diameter to the channel width is $1/18$, and the volume fraction is typically 5% in their study, whereas we consider two size ratios, 0.1 and 0.05, and a relatively low volume fraction 0.84%; (3) we examine the effects of the density ratio on the flow drag more systematically with the averaged equation and additional simulation data; and (4) the interphase drag and a different explanation of the particle migration are reported.

Our study is focused on the effects of the particles on the flow drag. It is well known that the addition of the polymer or the fiber can bring about drag reduction in the turbulent pipe or channel flows [33,34], but it remains an open question whether the addition of spherical particles has a similar drag-reduction effect. Radin *et al.* [35] summarized the previous experimental works, and observed that the data on the two-phase flow were conflicting: Some works showed a significant drag reduction but others showed no drag reduction. Radin *et al.* [35] provided some possible reasons for the inconsistency such as the incorrect definition of the friction factor for the suspension, the defects in the experimental setup (e.g., downward slope of the pipe, insufficient entrance length), and the effects of the electrostatic force. Radin *et al.* [35] conjectured that the drag reduction in gas-solid suspensions was due to a delayed and extended laminar-to-turbulent transition region probably caused by interparticle electrostatic forces which had the effect of inhibiting particle and fluid motion and hence stabilizing the viscous behavior and yielding a larger apparent viscosity. On the other hand, the charged particles adhering to the tube wall could increase the wall roughness and thereby the flow resistance. Radin *et al.* [35] concluded that the spherical particles in the liquid-solid suspension had no drag-reduction effect, whereas the experiments of Bari and Yunus [36] showed pronounced drag reduction due to the addition of the particles in the liquid. In numerical simulations, Zhao *et al.* [37] observed more than 10% drag reduction by the spherical particles in their simulations based on the point-particle model, and the reason was attributed to the attenuation in the fluid Reynolds stress.

The rest of the paper is organized as follows: The numerical method is outlined in Sec. II, and the method is validated in Sec. III. In Sec. IV, the results on the fluid-phase statistics, the solid-phase statistics, and the discussion on the particle effects on the flow drag are presented. The concluding remarks are given in Sec. V.

II. NUMERICAL METHOD

A. Flow simulation

A schematic diagram of the channel flow is shown in Fig. 1. The no-slip velocity boundary condition is imposed on the channel walls (i.e., the boundaries normal to the y axis) and the periodic boundary condition is imposed in both streamwise (x axis) and spanwise (z axis) directions. The corresponding velocity components in the (x,y,z) direction are $\mathbf{u} = (u,v,w)$, respectively. We denote the half width of the channel as H.

We take H as the characteristic length and the friction velocity u_τ as the characteristic velocity for the nondimensionalization scheme. The friction velocity is defined as $u_\tau = \sqrt{\tau_w/\rho_f}$, with τ_w being the mean shear stress on the walls, and ρ_f the fluid density. Thus, the Reynolds number is defined as $\mathrm{Re}_\tau = u_\tau H/\nu$, where ν is the fluid kinematic viscosity. The pressure gradient is kept constant in our simulations, implying $-\frac{dp_e}{dx} = \frac{\tau_w}{H}$ from the force balance for

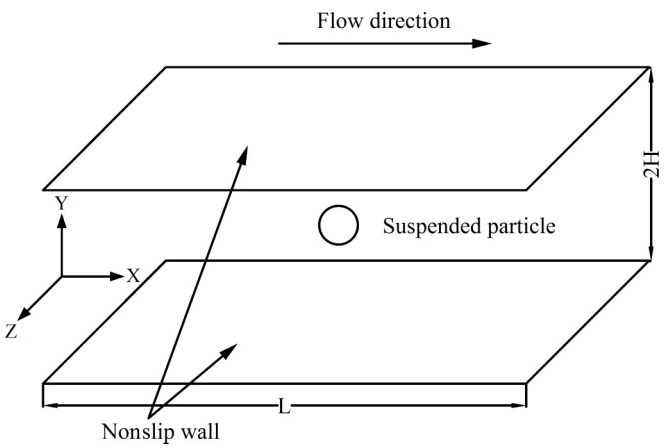

FIG. 1. Geometry model of channel. Schematic diagram of the channel flow, with x, y, and z representing the streamwise, transverse and spanwise coordinates, respectively.

the suspension flow at the statistically stationary state, and it follows that the dimensionless pressure gradient is 1. We note that the pressure gradient is applied to both fluid and solid domains.

B. Direct-forcing fictitious domain method

A parallel direct-forcing fictitious domain method (DF-FD) is employed for the simulation of the particle-laden turbulent channel flow. The fictitious domain (FD) method for the particulate flows was originally proposed by Glowinski *et al.* [38]. The key idea of this method is that the interior of the particles is filled with the fluids and the inner fictitious fluids are constrained to satisfy the rigid body motion through a pseudo body force, which is introduced as a distributed Lagrange multiplier in the FD formulation (Glowinski *et al.* [38]). In the following, we describe the DF-FD method briefly, and the reader is referred to Yu and Shao [39] for further details.

For simplicity of description, we will consider only one spherical particle in the following exposition. The particle density, volume and moment of inertia, translational velocity, and angular velocity and position are denoted by ρ_s, V_p, J, $\mathbf{U}$, $\boldsymbol{\omega}_p$, and $\mathbf{X}_p$, respectively. Let $P(t)$ represent the solid domain and Ω the entire domain including interior and exterior of the solid body. By introducing the following scales for the nondimensionalization, H for length, u_τ for velocity, H/u_τ for time, $\rho_f u_\tau^2$ for the pressure, and $\rho_f u_\tau^2/H$ for the pseudo body force per unit volume, the dimensionless FD formulation for the incompressible fluids and the spherical particles can be written as follows:

$$\frac{\partial \mathbf{u}}{\partial t} + \mathbf{u}\cdot\nabla\mathbf{u} = \frac{\nabla^2\mathbf{u}}{\mathrm{Re}_\tau} - \nabla p + 1 + \lambda \ \text{ in } \Omega, \tag{1}$$

$$\mathbf{u} = \mathbf{U} + \omega_\mathbf{p}\times\mathbf{r} \ \text{ in } P(t), \tag{2}$$

$$\nabla\cdot\mathbf{u} = 0 \ \text{ in } \Omega, \tag{3}$$

$$(\rho_r - 1)V_p^*\left(\frac{d\mathbf{U}}{dt} - \mathrm{Fr}\frac{\mathbf{g}}{g}\right) = -\int_P \boldsymbol{\lambda}\, d\mathbf{x}, \tag{4}$$

$$(\rho_r - 1)J^*\frac{d\omega_p}{dt} = -\int_P \mathbf{r}\times\boldsymbol{\lambda}\, d\mathbf{x}. \tag{5}$$

In the above equations, $\mathbf{u}$ represents the fluid velocity, p the fluid pressure after excluding the mean pressure gradient, the term "1" the mean pressure gradient, $\boldsymbol{\lambda}$ the pseudo body force that is defined in the solid domain $P(t)$, $\mathbf{r}$ the position vector with respect to the mass center of the particle, ρ_r the particle-fluid density ratio defined by $\rho_r = \rho_s/\rho_f$, Fr the Froude number defined here by $\mathrm{Fr} = gH/u_\tau^2$, V_p^* the dimensionless particle volume defined by $V_p^* = V_p/H^3$, and J^* the dimensionless moment of inertia defined by $J^* = J/\rho_s H^5$.

A fractional-step time scheme is used to decouple the system (1)–(5) into the following two subproblems.

Fluid subproblem for $\mathbf{u}^*$ and p:

$$\frac{\mathbf{u}^* - \mathbf{u}^n}{\Delta t} - \frac{1}{2}\frac{\nabla^2\mathbf{u}^*}{\mathrm{Re}_\tau} = -\nabla p + 1 - \frac{1}{2}[3(\mathbf{u}\cdot\nabla\mathbf{u})^n - (\mathbf{u}\cdot\nabla\mathbf{u})^{n-1}] + \frac{1}{2}\frac{\nabla^2\mathbf{u}}{\mathrm{Re}_\tau} + \boldsymbol{\lambda}^n, \tag{6}$$

$$\nabla\cdot\mathbf{u}^* = 0. \tag{7}$$

A finite-difference-based projection method on a homogeneous half-staggered grid is used for the solution of the above fluid subproblem. All spatial derivatives are discretized with the second-order central difference scheme.

Particle subproblem for $\mathbf{U}^{n+1}$, $\boldsymbol{\omega}_p^{n+1}$, $\boldsymbol{\lambda}^{n+1}$, and $\mathbf{u}^{n+1}$:

$$\rho_r V_p^*\frac{\mathbf{U}^{n+1}}{\Delta t} = (\rho_r - 1)V_p^*\left(\frac{\mathbf{U}^n}{\Delta t} - \mathrm{Fr}\frac{\mathbf{g}}{g}\right) + \int_P\left(\frac{\mathbf{u}^*}{\Delta t} - \boldsymbol{\lambda}^n\right)d\mathbf{x}, \tag{8}$$

$$\rho_r\frac{J^*\omega_p^{n+1}}{\Delta t} = (\rho_r - 1)\frac{J^*\omega_p^n}{\Delta t} + \int_P r\times\left(\frac{\mathbf{u}^*}{\Delta t} - \boldsymbol{\lambda}^n\right)d\mathbf{x}. \tag{9}$$

Note that the above equations have been reformulated so that all the right-hand-side terms are known quantities and consequently the particle velocities $\mathbf{U}^{n+1}$ and $\boldsymbol{\omega}_p^{n+1}$ are obtained without iteration. Then $\boldsymbol{\lambda}^{n+1}$ defined at the Lagrangian nodes are determined from

$$\boldsymbol{\lambda}^{n+1} = \frac{\mathbf{U}^{n+1} + \boldsymbol{\omega}_p^{n+1}\times\mathbf{r} - \mathbf{u}^*}{\Delta t} + \boldsymbol{\lambda}^n. \tag{10}$$

Finally, the fluid velocities $\mathbf{u}^{n+1}$ at the Eulerian nodes are corrected from

$$\mathbf{u}^{n+1} = \mathbf{u}^* + \Delta t(\boldsymbol{\lambda}^{n+1} - \boldsymbol{\lambda}^n). \tag{11}$$

In the above manipulations, the trilinear function is used to transfer the fluid velocity from the Eulerian nodes to the Lagrangian nodes, and the pseudo body force from the Lagrangian nodes to the Eulerian nodes.

For our parallel algorithm, the domain decomposition is chosen as the parallel-computation strategy and Message Passing Interface (MPI) is used to transfer data among subdomains. The reader is referred to Yu *et al.* [32] for the details on the parallel-computation algorithm.

C. Collision model

A particle-particle collision model is required to prevent the mutual penetration of particles. We adopt the following simple soft-sphere collision model:

$$\mathbf{F}_{ij} = F_0(1 - d_{ij}/d_c)\mathbf{n}_{ij}, \tag{12}$$

where $\mathbf{F}_{ij}$, d_{ij}, and $\mathbf{n}_{ij}$ are the repulsive force acting on particle j from particle i, the gap distance and the unit normal vector pointing from the center of particle i to that of particle j, respectively. d_c represents a cutoff distance and the repulsive force is activated when $d_{ij} < d_c$. F_0 is the magnitude of the force at contact. We set $d_c = h$ (h being the fluid mesh size),

TABLE I. Parameter settings for the simulations of particle-laden turbulent channel flows.

Case	a/H	ρ_r	Re_τ	N_p	ϕ_0	Domain size	Grid number	Δt
Particle-free			180			$8H \times 2H \times 4H$	$512 \times 128 \times 256$	0.0002
Particle-laden A	0.05	1.0	180	1024	0.84%	$8H \times 2H \times 4H$	$512 \times 128 \times 256$	0.0002
Particle-laden B	0.05	10.42	180	1024	0.84%	$8H \times 2H \times 4H$	$512 \times 128 \times 256$	0.0002
Particle-laden C	0.05	104.2	180	1024	0.84%	$8H \times 2H \times 4H$	$512 \times 128 \times 256$	0.0001
Particle-laden D	0.1	1.0	180	128	0.84%	$8H \times 2H \times 4H$	$512 \times 128 \times 256$	0.0002
Particle-laden E	0.1	10.42	180	128	0.84%	$8H \times 2H \times 4H$	$512 \times 128 \times 256$	0.0002
Particle-laden F	0.1	104.2	180	128	0.84%	$8H \times 2H \times 4H$	$512 \times 128 \times 256$	0.0001
Particle-laden G	0.05	10.42	180	5	0.0041%	$8H \times 2H \times 4H$	$512 \times 128 \times 256$	0.0002
Particle-laden H	0.05	10.42	180	100	0.082%	$8H \times 2H \times 4H$	$512 \times 128 \times 256$	0.0002

and $F_0 = 10^3$. The motions of the particles due to the collision force (12) and due to the hydrodynamic force [(8) and (9)] are handled separately with a fractional-step scheme. The time step for the collision model is set to be one-tenth of the latter (i.e., $\Delta t/10$) to circumvent the stiffness problem arising from the explicit integration scheme with a large value of F_0, as suggested by Glowinski *et al.* [38]). The collision between a particle and a wall is treated similarly as two particles with the coefficient F_0 in (12) doubled. This collision model (12) has been used widely in the interface-resolved numerical simulations of particle-laden flows [19,38] due to its simplicity. We note that more sophisticated collision models have been proposed by Kempe and Fröhlich [40] and de Motta *et al.* [41]. The particle volume fraction in the present study is low (0.84%), and the collision model is expected not to affect the results qualitatively, as shown in our recent work on the particle-laden duct flow at the particle volume fraction of 2.36% [42]. In one sense, one may think that there exist physically short-range repulsive forces between the particles (and between the particles and the wall) in our fluid-solid system.

D. Parameter settings

Throughout this study the friction Reynolds number Re_τ is set to 180. The average particle volume fraction is $\phi_0 = 0.84\%$, unless otherwise specified. Two particle sizes are considered: $a/H = 0.05$ and 0.1, here a being the particle radius. Three particle-fluid density ratios are chosen: $\rho_r = 1.0$, 10.42, and 104.2, in order to examine the density ratio effects. The variation of the particle density could change both the particle-inertia and the particle-settling effects. But for simplicity, we decouple the two effects and do not consider the settling effect (or gravity effect), so that the density ratio is assumed to only reflect the particle inertia. The Froude number (Fr) is zero, since the gravity effect is not considered. The particles are randomly distributed into the fully developed single-phase flow at the initial time with initial velocities equal to the local fluid velocities at the center of the particles.

In the present study, the computational domain is $[0,8H] \times [-H,H] \times [0,4H]$, and the grid resolution is $512 \times 128 \times 256$, corresponding to the mesh size $h = H/64$. The time step is $0.0002\ H/u_\tau$ for $\rho_r \leqslant 10.42$ and $0.0001\ H/u_\tau$ for $\rho_r = 104.2$. A smaller time step for a larger density ratio is required due to numerical stability. The parameter settings are presented in Table I.

The flow statistics are obtained from the averaging of the data in the real fluid domain outside the particle boundaries over typically 50 nondimensional time units after the statistically stationary stage is reached. The particle-phase statistics are obtained from the data at the fictitious fluid points inside the particle boundaries.

III. VALIDATION

The accuracy of our code for the single-phase turbulent channel flow was validated in the previous studies [23,32] by comparing the results to the highly accurate pseudospectral simulations. For the turbulent particle-laden channel flows, no benchmark data are available to validate the accuracy. In a recent study [23], we have compared our results to lattice-Boltzmann simulations using interpolated bounce back at the fluid-solid interfaces, for neutrally buoyant particles. The comparisons show that the two completely different numerical approaches (one conventional and the second mesoscopic) yield quantitatively similar results in general.

For our simulation case of $a/H = 0.05$, there are only 3.2 meshes per particle radius, and one may question whether such mesh resolution is high enough to ensure acceptable accuracy. With the parallel code, a mesh-convergence test has been conducted for $a/H = 0.05$ and $\rho_r = 104.2$ [32], in which case the RMS (root-mean-square) velocities deviate significantly from those for the particle-free case. It was shown that the results on the RMS velocities for two meshes $h = a/3.2$ and $h = a/6.4$ agreed well with each other, with the maximum relative error at the peaks of the streamwise RMS velocities being around 3% [32].

IV. RESULTS AND DISCUSSION

A. Fluid-phase statistics

The results on the fluid-phase mean and RMS velocities for $a/H = 0.05$ and $\phi_0 = 0.84\%$ were reported in our previous work [32], and consequently are not presented here. Figure 2 shows the mean fluid velocity profiles for $a/H = 0.1$. One can observe that the flow rate does not change monotonically as the density ratio increases from unity to 104.2. For both cases of $a/H = 0.05$ and $a/H = 0.1$, the flow rates are lowest at $\rho_r = 10.42$, and show the trend of returning back toward that of the single-phase flow for $\rho_r = 104.2$. The drag coefficient can be defined as the ratio of the flow rate of the fluid-solid mixture to the pressure gradient. It will be shown that the solid-phase

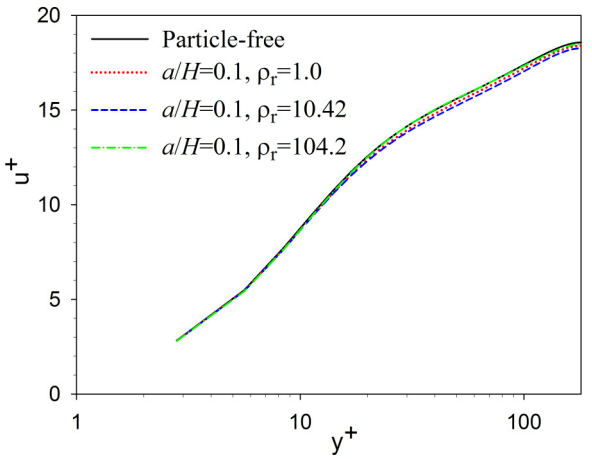

FIG. 2. Mean fluid velocity profiles for $a/H = 0.1$ at different density ratios.

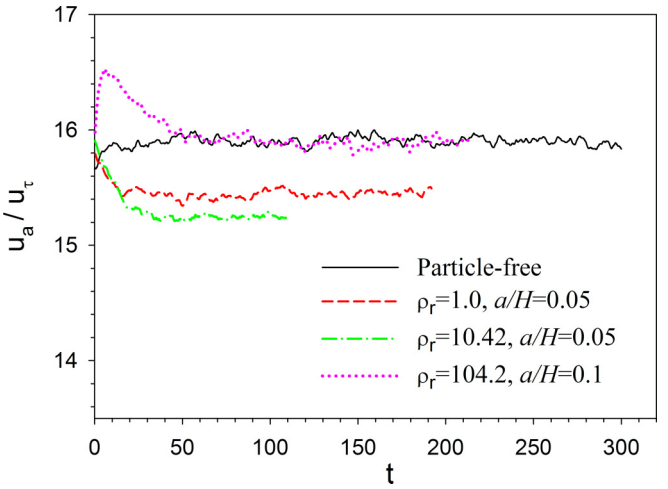

FIG. 3. Evolutions of the fluid-phase flow rate (average velocity) for different density ratios.

contribution to the mixture flow rate is almost independent of the density ratio (Table II), and therefore the two-phase flow rate and the fluid-phase flow rate change with the density ratio in qualitatively the same way. Since the pressure gradient is fixed, our results indicate that the flow drag is largest for the density ratio of the order of 10. Our results are consistent with those of Fornari *et al.* [31] who observed that the flow drag was enhanced slightly as the density ratio was increased from unity to 10. Significant drag reduction by the addition of the spherical particle was observed in the point-particle simulations [37], but not in our interfaced-resolved direct simulations. Whether the point particles can cause drag reduction is still in debate, as pointed out by one anonymous referee of the present paper. For the classic point-particle model in which the particle resultant force acts back on the fluids via spreading of the force on the closest Eulerian grid points, the method is sensitive to the grid resolution and lack of numerical convergence to grid refinements [43]. A number of different approaches have been developed for two- and four-way coupling simulations that are shown to be grid independent and accurate at a moderate computational cost [44–46]. Further studies based on the simulations with these more accurate methods or the interface-resolved direct simulations for small particles are required to confirm whether the significant drag reduction can be produced by the spherical particles, since the experimental results in the literature were inconsistent, as mentioned in the Introduction.

The mean velocity profiles in Fig. 2 are obtained for the statistically stationary stage. Figure 3 shows the evolutions of the fluid-phase flow rate for different density ratios. For all cases, the initial flow field is the fully developed single-phase turbulence, and the particles are initially distributed uniformly in the channel with the velocity being equal to the local fluid velocity at the particle center. As shown in Fig. 3, for $\rho_r = 1$ and 10.42, the flow rates decrease with time until the stationary stages are reached, whereas for $\rho_r = 104.2$ the flow rate increases rapidly after the particles are added, and then decreases slowly to a statistically stationary value. Thus we observe a significant drag reduction at the transient state for considerably large particle inertia, which may indicate that the drag reduction in some previous experiments might be caused by the unsteady effect such as the delay in the turbulence transition due to the particles.

The root-mean-square (RMS) values of the fluid velocity fluctuations in all three directions for $a/H = 0.1$ and the fluid Reynolds shear stresses for both $a/H = 0.05$ and $a/H = 0.1$ are plotted in Fig. 4. For $\rho_r = 1.0$ and 10.42, the particle addition enhances the transverse and spanwise RMS velocities near the wall and attenuates the peak streamwise RMS velocity, as observed in the previous simulations for the neutrally buoyant case [19,22,23]. When the density ratio reaches the order of 100, all RMS velocity components and the Reynolds shear stress are attenuated roughly at any transverse position, particularly for $a/H = 0.05$, as a result of significant

TABLE II. Contributions of the individual stresses in Eq. (20) to the flow drag. The relative differences between the bulk velocities for the particle-laden and particle-free cases are provided in the column of the bulk velocity.

	u_b^+ $(\frac{2}{\sqrt{f}})$	C_T	C_{fR}	C_{pR}	C_{pI}	C_{pu}	$C_{fR}+C_{pR}$
Particle-free	15.96	60.0	44.04				
$a/H = 0.05$, $\rho_r = 1.0$	15.53 (−2.69%)	59.93	43.97	0.32	0.27	0.14	44.29
$a/H = 0.05$, $\rho_r = 10.42$	15.25 (−4.45%)	59.83	40.89	2.76	1.08	0.14	43.65
$a/H = 0.05$, $\rho_r = 104.2$	15.77 (−1.19%)	59.87	28.09	13.82	2.33	0.13	41.91
$a/H = 0.1$, $\rho_r = 1.0$	15.79 (−1.07%)	59.91	43.28	0.23	0.77	0.14	43.51
$a/H = 0.1$, $\rho_r = 10.42$	15.65 (−1.94%)	59.80	41.54	1.69	1.06	0.14	43.23
$a/H = 0.1$, $\rho_r = 104.2$	15.91 (−0.31%)	59.82	38.40	4.16	1.48	0.14	42.56

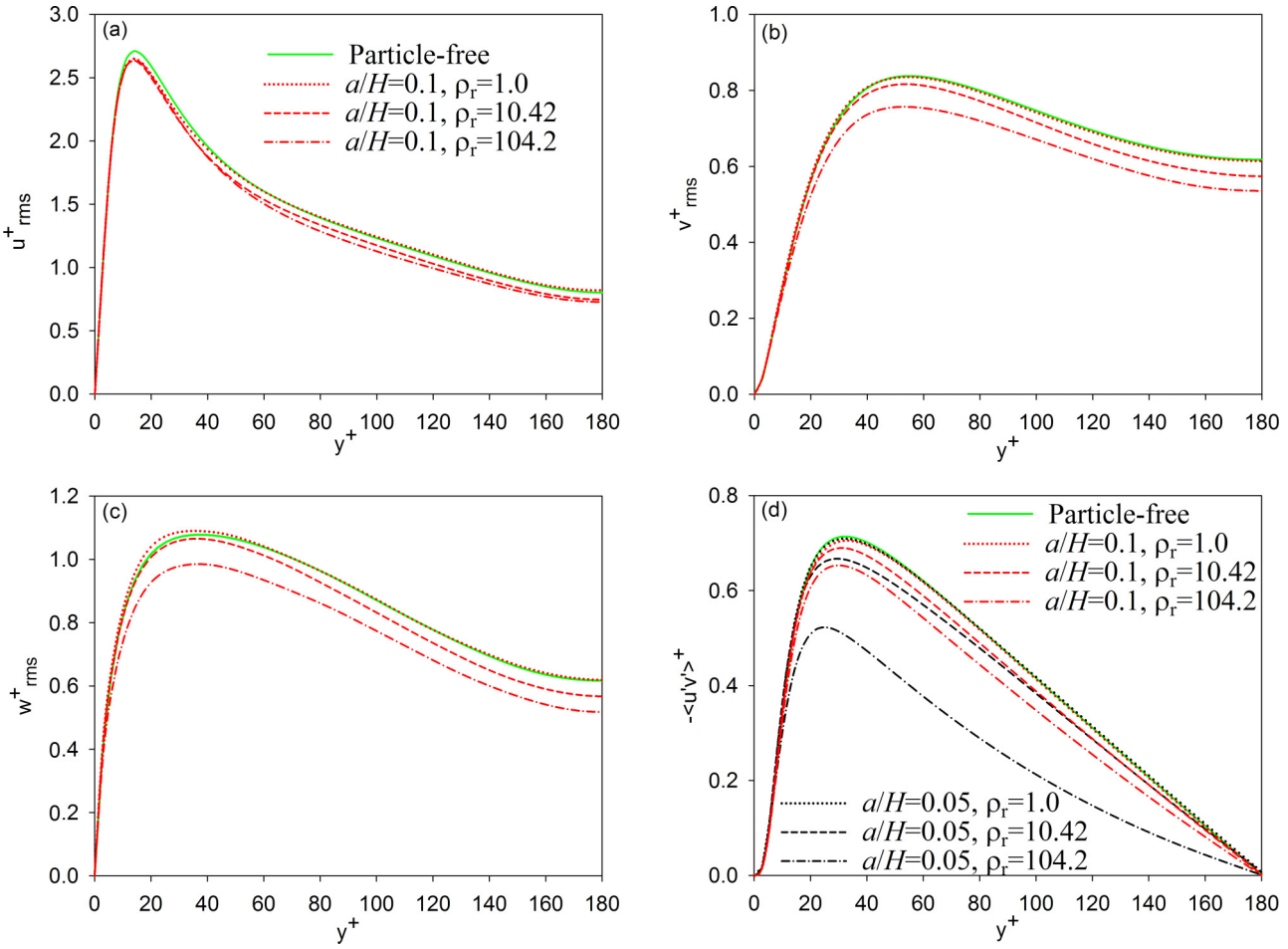

FIG. 4. Fluid RMS velocity components: (a) streamwise, (b) transverse, (c) spanwise; and (d) the fluid Reynolds shear stress.

suppression of the large-scale vortices by the particles with large inertia (i.e., large density ratio) [32].

B. Solid-phase statistics

The solid-phase mean velocity profiles for both $a/H = 0.05$ and $a/H = 0.1$ are plotted in Fig. 5, and the fluid mean velocities are also plotted for comparison. The solid-phase statistics are computed with the data on the grids covered by the particles. For $\rho_r = 1.0$, the fluid and solid mean velocities are close to each other except at the near-wall region where the solid velocities are larger; the slip at the wall region was observed previously [22,23]. For $\rho_r \geqslant 10.42$, there exists a critical distance from the wall, below which the solid mean velocity is larger, and above which the fluid mean velocity is larger. This means that the particle inertia makes the particles lag the high-speed fluid and lead the low-speed fluid on average. For $\rho_r = 104.2$, the particle inertia is so large that the particles are not sensitive to the local fluid velocity and their velocities are roughly constant across the channel. Generally, the slip velocity increases with increasing density ratio and particle size.

The solid-phase RMS velocities and kinematic Reynolds shear stresses (here meaning $\langle -u_p' v_p' \rangle$ without the density) for all cases are plotted in Fig. 6. For the same particle volume fraction, the effects of the smaller particles are more significant because the number of the particles (and total particle-fluid interface area) is much higher. The intensity of solid-phase velocity fluctuations generally decreases with increasing particle density, except that the streamwise RMS velocity and $\langle -u_p' v_p' \rangle$ in the near-wall region are largest at the particle density ratio of the order of 10. The solid-phase RMS velocities are larger than those of the fluid in the near-wall region due to the collision between the particles and the wall. Our results on the streamwise particle RMS velocity are consistent with those of Fornari *et al.* [31] for $\rho_r = 104.2$, $a/H = 1/18$, and $\phi = 5\%$, but the results on the transverse (wall-normal) RMS velocity are inconsistent: Our results show that the transverse RMS velocity for $\rho_r = 10.42$ is smaller than that for $\rho_r = 1$ over the entire domain, whereas their results showed that at around $y = 0.15H$ (i.e., $y^+ = 27$), the transverse RMS velocity for $\rho_r = 10.42$ is larger than that for $\rho_r = 1$. A possible reason for the discrepancy is that the particle collision interactions are strongest at the density ratio of order 10, and stronger particle collision interactions at a higher particle volume fraction increase the transverse RMS velocity for $\rho_r = 10.42$ more significantly in the simulations of Fornari *et al.* [31].

Fornari *et al.* [31] observed the particle migration toward the channel centerline at the density ratio of the order of 10, and proposed a reasonable explanation: the particle collision leads to the lateral motion of the particles and then a net particle

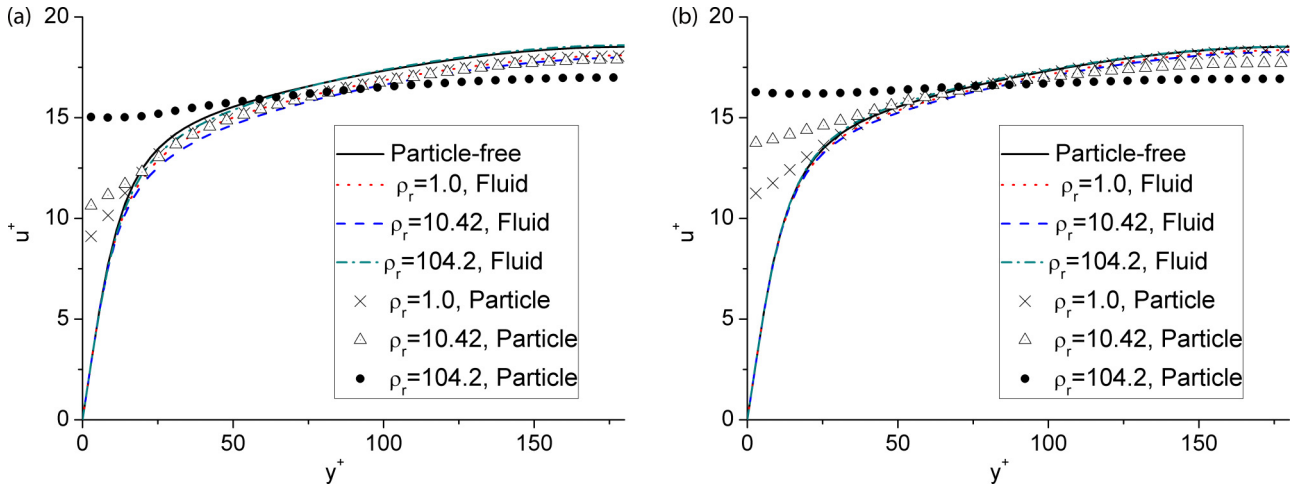

FIG. 5. Fluid and solid-phase mean velocity profiles at different density ratios for (a) $a/H = 0.05$ and (b) $a/H = 0.1$.

diffusion toward the centerline due to wall confinement. There is no migration for $\rho_r = 1$ because the particles response to the fluid motion rapidly after the collision, and no migration for $\rho_r = 104.2$ because the particle inertia is so strong that the particles hardly respond to the fluid action and the velocity difference for the particles in neighboring layers is small (Fig. 5), which reduces the possibility of the particle collision. Our results on the distribution of the local particle volume fraction are presented in Fig. 7, and significant migration can be observed for $a/H = 0.05$ and $\rho_r = 10.42$. For the same

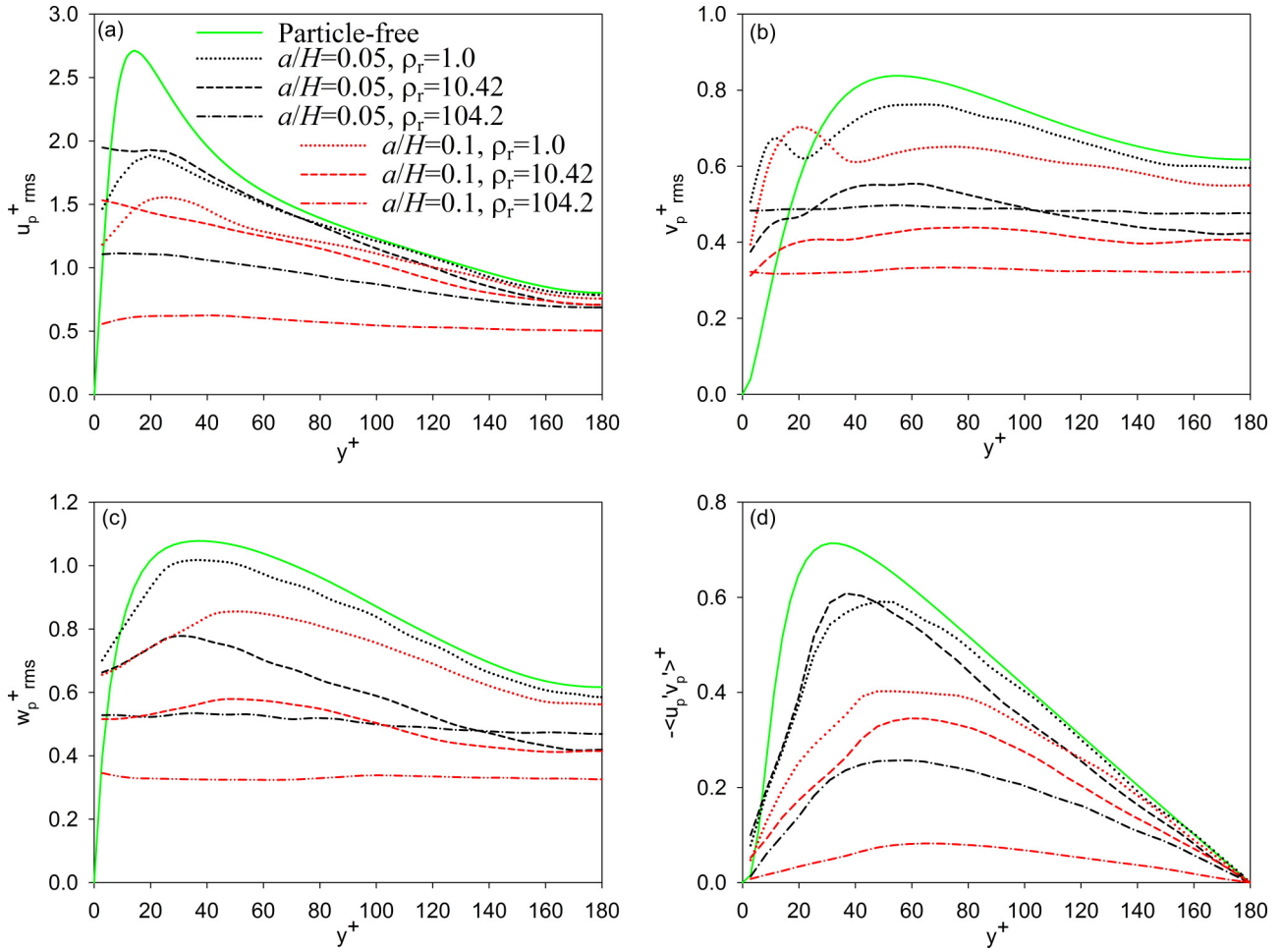

FIG. 6. Solid-phase RMS velocity fluctuations: (a) streamwise, (b) transverse, and (c) spanwise; and (d) the solid-phase kinematic Reynolds shear stress. The single-phase flow statistics are shown for comparison.

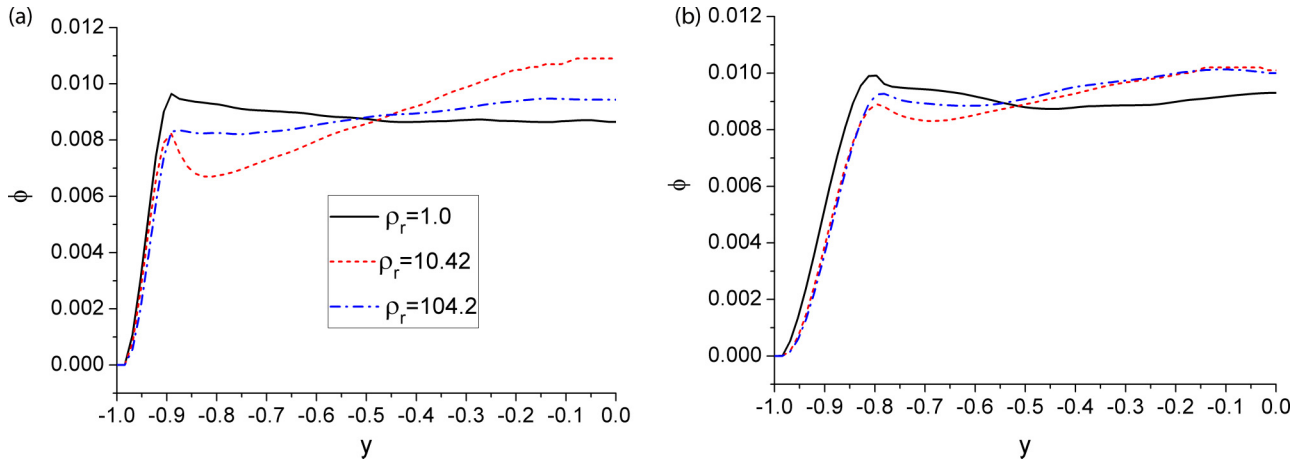

FIG. 7. Distribution of the local particle volume fraction for (a) $a/H = 0.05$ and (b) $a/H = 0.1$.

particle volume fraction, the particle number for $a/H = 0.05$ is 8 times that for $a/H = 0.1$; consequently the collision frequency is much lower for $a/H = 0.1$, which may explain why the particle migration is less pronounced for $a/H = 0.1$, compared to $a/H = 0.05$.

Although the particle collision can account for the particle migration toward the channel centerline at the density ratio of order 10, it is not clear whether the particle-turbulence interactions would play a role. For the wall-bounded turbulent flows, a sharp rise in the particle volume fraction near the wall was commonly observed (e.g., Reeks [47]; Uhlmann [16]; Marchioli and Soldati [48]; Sardina *et al.* [49]). The main mechanism for this particle preferential accumulation was recognized as turbophoresis, an average migration of particles in the direction opposite to gradients in the turbulence intensity. For an individual particle, this means that it is less probable to receive the necessary momentum driving it from a region of low turbulence intensity toward a high-intensity region than vice versa (Uhlmann [16]). From Fig. 7, the turbophoresis seems absent for the neutrally buoyant case. To examine whether the turbophoresis (or turbulence-induced particle migration) occurs for $\rho_r = 10.42$ and $a/H = 0.05$, two cases of lower particle concentrations ($\phi_0 = 0.0041\%$ and 0.082%, corresponding to the particle number $N_p = 5$ and 100) are simulated for a long time (more than 500 time units). The concentration distributions are shown in Fig. 8. The collisions between the particles seldom take place for $N_p = 5$; however, similar migration can still be observed in Fig. 8, indicating that the turbulence plays an important role in the particle migration. The concentration distribution is more inhomogeneous for $N_p = 1024$ (i.e., $\phi_0 = 0.84\%$), implying that the particle collision promotes the particle migration. Thus we can conclude that both particle collision and particle-turbulence interactions are responsible for the particle migration toward the channel center in a statistical sense for $a/H = 0.05$ and $\rho_r = 10.42$.

C. Discussion on the flow drag

In this subsection, we will explore the mechanisms for the particle effects on the flow drag. The friction coefficient for the channel flow can be defined by

$$f = \frac{\left(-\frac{dp_e}{dx}\right)4H}{\rho_f u_b^2} = 4\left(\frac{u_\tau}{u_b}\right)^2, \tag{13}$$

where u_b represents the bulk velocity of the two-phase flow. In Eq. (13), the following relationship is used:

$$\left(-\frac{dp_e}{dx}\right) = \frac{\tau_w}{H} = \frac{\rho_f u_\tau^2}{H}. \tag{14}$$

The following energy balance equation holds for both single-phase and particle-laden flows:

$$\left(-\frac{dp_e}{dx}\right)u_a = \rho_f \bar{\varepsilon}, \tag{15}$$

where $\bar{\varepsilon}$ is the mean viscous dissipation rate, defined by $\bar{\varepsilon} = \nu\overline{\frac{\partial u_i}{\partial x_j}\frac{\partial u_i}{\partial x_j}}$. Equation (15) means that the energy input rate is equal to the energy dissipation rate. From Eq. (15), for the simulations with the constant flow rate, the increase in the viscous dissipation rate implies the increase in the flow resistance, whereas for the simulations with the constant pressure gradient, the increase in the viscous dissipation rate implies

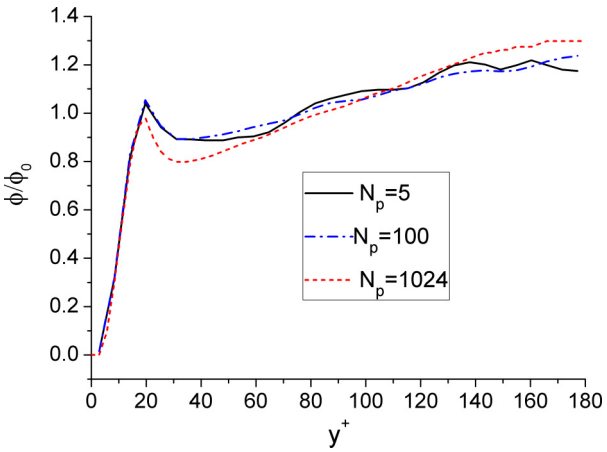

FIG. 8. Distribution of the local particle volume fraction normalized by the average particle volume fraction for $a/H = 0.05$ and $\rho_r = 10.42$.

the decrease in the flow resistance. Thus, when we say we are examining the relationship between the viscous dissipation rate and the flow resistance, we mean the dissipation rate normalized by the average velocity, which is proportional to the friction coefficient. From the physical point of view, the presence of particles causes additional viscous dissipation in the near-surface region (Lucci *et al.* [7]), which has dual effects on the flow drag. On the one hand, more viscous dissipation means higher viscosity of the suspension mixture and thereby larger flow drag. On the other hand, more viscous dissipation leads to suppression of the large-scale quasistreamwise vortices which are primarily responsible for the drag enhancement of turbulence with respect to the laminar flow, and thereby a lower flow resistance. The competition of these two effects may give rise to the results observed earlier: The flow drag first increases and then decreases with increasing density ratio.

The above argument based on the viscous dissipation rate provides one perspective for understanding the particle effects on the flow drag. In the following, we attempt to provide alternative explanations from the averaged momentum equation. In the Appendix, we derive three equations for the fluid mean velocity, based on the spatial averaging theorem.

The first is related to the solid-phase Reynolds and inner stresses [Eq. (A13)]:

$$\underbrace{\varphi_f \mu \frac{d\langle u_f\rangle}{dy}}_{\tau_{fV}} + \underbrace{\varphi_s \langle \sigma_p\rangle_{xy}}_{\tau_{pI}} + \underbrace{\varphi_f \rho_f \langle -u_f' v_f'\rangle}_{\tau_{fR}} + \underbrace{\varphi_s \rho_s \langle -u_p' v_p'\rangle}_{\tau_{pR}} = \underbrace{\tau_w\left(1-\frac{y}{H}\right)}_{\tau_T}, \tag{16}$$

where u and v are the local velocity components in the x and y directions, respectively, with the subscript "f" meaning the fluid phase and "p" or "s" meaning the solid phase, σ_p is the solid inner stress, φ_f and φ_s are the fluid and solid volume fractions at a given y position, and the brackets represent the phase averaging, i.e., $\langle A_i\rangle = \frac{1}{V_i}\int_{V_i} A_i dV$, in which the subscript "i" represents the fluid phase or the solid phase. The five terms in Eq. (16) represent the fluid viscous stress τ_{fV}, the particle inner stress τ_{pI}, the fluid Reynolds stress τ_{fR}, the particle Reynolds stress τ_{pR}, and the total stress τ_T, respectively. Note that here the particle Reynolds stress means the solid-phase Reynolds stress; namely, the velocities on the Eulerian grids inside the particle boundaries rather than the particle translational velocities are used for the computation of the particle Reynolds stress.

Equation (16) was derived by Picano *et al.* [22] who used the phase indicator function for spatial averaging, and in the Appendix we derive it by using a different averaging technique, i.e., the spatial averaging theorem. Equation (16) indicates that the total shear stress of the two-phase system for the channel flow decreases linearly from the wall to the centerline, as in the case of single-phase flow. Since the pressure gradient is kept constant in our simulations, the mean wall stress τ_w is the same for all cases [Eq. (14)]. Then the reduction in the particle inner stress, the fluid Reynolds shear stress, or the solid Reynolds shear stress can lead to the increase in the fluid shear rate and thereby the increase in the fluid velocity, and thus the reduction in the flow drag. In the following, we will examine the behavior of the individual stresses and their contributions to the flow drag at different density ratios.

Figure 9 shows the profiles of the fluid viscous stress, the fluid Reynolds stress, the particle Reynolds stress, and the particle inner stress for $\rho_r = 1$, 10.42, and 104.2. The stresses are normalized by $\rho_f u_\tau^2$. The particle inner stress is determined from Eq. (16). As the density ratio increases, the particle inner stress does not change significantly, while the particle Reynolds stress increases substantially. The particle inner stress has a peak near the wall, and decreases to zero as the position approaches the wall due to the depletion of the particle volume fraction in the near-wall region. Note that the local volume fraction is included in the definition of the stresses in Eq. (16). Since the particle volume fraction is low, the particle Reynolds stresses are much smaller than the fluid Reynolds stresses for $\rho_r = 1$, 10.42. However, for $\rho_r = 104.2$ and $a/H = 0.05$, the two Reynolds stresses are comparable, because the fluid Reynolds stress is decreased, while the particle Reynolds stress is increased, as the density ratio increases.

From Eq. (13), the friction coefficient for the channel flow is related to the ratio of the average velocity and the friction velocity. The friction velocity is determined from the wall shear force, which can be further determined from the pressure gradient. There are two ways to examine the effect of the particles on the flow drag: One is to keep the flow rate the same and compare the wall shear force, and the other is to keep the pressure gradient (i.e., wall shear force) the same and compare the flow rate. Fornari *et al.* [31] used the former, and we used the latter here. For the latter, one can derive the contributions of the individual stresses to the friction coefficient, as shown below.

Equation (16) can be rewritten as follows:

$$\frac{d\langle u_f\rangle}{dy} = \frac{1}{\varphi_f \mu}(\tau_T - \tau_{fR} - \tau_{pI} - \tau_{pR}), \tag{17}$$

The average velocity at a y position is obtained by integrating Eq. (17),

$$\langle u_f\rangle = \int_0^y \frac{1}{\varphi_f \mu}(\tau_T - \tau_{fR} - \tau_{pI} - \tau_{pR})d\xi. \tag{18}$$

The bulk (or average) velocity of the fluid-solid mixture can be calculated from

$$\begin{aligned} u_b &= \frac{1}{H}\int_0^H [\varphi_f\langle u_f\rangle + \varphi_s\langle u_s\rangle]dy \\ &= \frac{1}{H}\int_0^H \varphi_f \int_0^y \frac{1}{\mu\varphi_f}(\tau_T - \tau_{fR} - \tau_{pI} - \tau_{pR})d\xi dy \\ &\quad + \frac{1}{H}\int_0^H [\varphi_s\langle u_p\rangle]dy. \end{aligned} \tag{19}$$

The friction coefficient is related to the dimensionless stresses:

$$\frac{2}{\sqrt{f}} = \frac{u_b}{u_\tau} = \frac{1}{\mathrm{Re}_\tau}\int_0^{\mathrm{Re}_\tau} \varphi_f \int_0^{y^+} \frac{1}{\varphi_f}(\tau_T^+ - \tau_{fR}^+ - \tau_{pI}^+ - \tau_{pR}^+) \times d\xi^+ dy^+ + \frac{1}{\mathrm{Re}_\tau}\int_0^{\mathrm{Re}_\tau} [\varphi_s\langle u_s\rangle^+]dy^+, \tag{20}$$

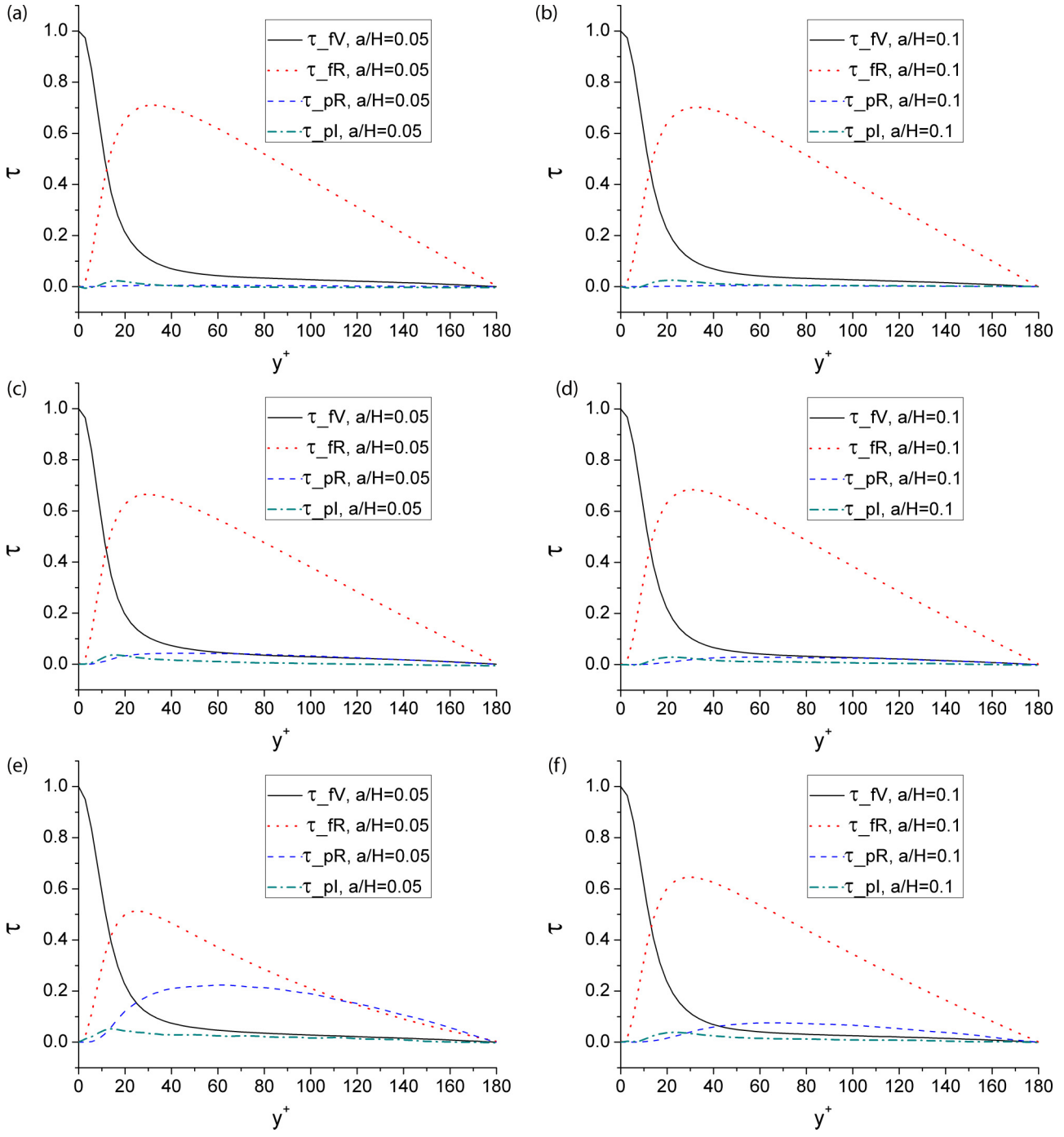

FIG. 9. Profiles of the fluid viscous stress τ_{fV}, the fluid Reynolds stress τ_{fR}, the particle Reynolds stress τ_{pR}, and the particle inner stress τ_{pI} defined in Eqs. (16) and (21) for (a),(b) $\rho_r = 1$, (c),(d) $\rho_r = 10.42$, and (e),(f) $\rho_r = 104.2$.

where the stresses are normalized by $\rho_f u_\tau^2$. Specifically, the normalized stresses have the following forms:

$$\tau_{fV}^+ = \varphi_f \frac{d\langle u_f^+ \rangle}{dy^+}, \quad \tau_{fR}^+ = \varphi_f \langle -u_f' v_f' \rangle^+,$$

$$\tau_{pR}^+ = \varphi_s \rho_r \langle -u_p' v_p' \rangle^+, \quad \text{and} \quad \tau_T^+ = \left(1 - \frac{y^+}{\mathrm{Re}_\tau}\right). \quad (21)$$

We define the terms of the total stress, the fluid Reynolds stress, the particle inner stress, the particle Reynolds stress, and the particle average velocity in Eq. (20) as C_T, C_{fR}, C_{pI}, C_{pR}, and C_{pu}, respectively, and their values and the dimensionless bulk velocity (i.e., $2/\sqrt{f}$) are presented in Table II. For the particle-free case, the total stress term is $\mathrm{Re}_\tau/3$ and is thus 60 for $\mathrm{Re}_\tau = 180$. For the particle-laden case, its value becomes slightly smaller due to the effect of the fluid volume fraction. The fluid Reynolds stress term decreases, while both particle Reynolds and inner stress terms increase, as the density ratio increases for the same particle size. The fluid and particle Reynolds stress terms change significantly, as the density

ratio changes from unity to 104.2, but interestingly, their sum (i.e., the total Reynolds stress of the fluid-solid mixture) does not change much, and actually decreases slightly with increasing density ratio. The particle velocity contribution is almost independent of the density ratio. Further, since the total Reynolds stress and particle inner stress terms are not sensitive to the density ratio, the flow drag is not sensitive to the density ratio. The results in Table II indicate that the increase in the flow drag (i.e., decrease in the flow rate) from $\rho_r = 1$ to $\rho_r = 10.42$ is mainly due to a larger amount of the increase in the particle total stress (sum of the particle Reynolds stress and inner stress) than the decrease in the fluid Reynolds stress. A smaller amount of the increase in the total particle stress than the decrease in the fluid Reynolds stress explains the decrease in the flow drag from $\rho_r = 10.42$ to $\rho_r = 104.2$. In other words, the flow drag reaches maximum at the density ratio of order 10 because the sum of the fluid Reynolds stress, the particle Reynolds stress, and the particle inner stress terms reaches maximum. We note that the contribution of the particle inner stress is important for the nonmonotonic change of the drag coefficient.

The second equation for the fluid mean velocity is related to the interphase hydrodynamic force [Eq. (A6)],

$$\frac{d}{dy}\left(\varphi_f \mu \frac{d\langle u_f\rangle}{dy}\right) + \varphi_f\left(-\frac{dp_e}{dx}\right) + \frac{d}{dy}(\varphi_f \rho_f \langle -u_f' v_f'\rangle) - \frac{F_x}{V} = 0, \tag{22}$$

where F_x is the interphase average drag force on the particles. From Eq. (A7), the interphase hydrodynamic force is related to the particle total stress:

$$\frac{d(\tau_{pR} + \tau_{pI})}{dy} + \varphi_s\left(-\frac{dp_e}{dx}\right) + \frac{F_x}{V} = 0. \tag{23}$$

Since the pressure gradient is constant in our simulations, the gradient of the particle total stress reflects the interphase drag force. As discussed earlier, the drag-reduction effect due to the decrease in the Reynolds shear stress is counteracted by the drag-enhancement effect due to the increase in the particle total stress, as the density ratio increases. Equations (22) and (23) imply that the drag-enhancement effect can also be attributed to the increase in the interphase drag force.

The drag formula modeling the interphase drag force is most important for the engineering multiphase flow models such as the point-particle model and the two-fluid model. In the following, we attempt to calculate the interphase drag force from Eq. (22) (referred to as the balance theory since it is a force balance equation for the fluid at the statistically stationary state), and examine whether the empirical drag formula can qualitatively predict the interphase drag for the turbulent particle-laden channel flow. The slip velocity is required in the drag formula. For the point-particle model, the slip velocity between the individual particle and the fluid is employed, and for the two-fluid model, the slip velocity between the phase-averaged velocities is adopted. For the freely moving finite-size particle, the slip velocity between the individual particle and the fluid cannot be defined unambiguously; consequently, we here take the difference between the phase-averaged velocities as the slip velocity.

Equation (22) normalized by the friction velocity u_τ and half channel width H becomes

$$\frac{F_x^+}{V^+} = \left[\mathrm{Re}_\tau \frac{d}{dy^+}\left(\varphi_f \frac{d\langle u_f\rangle^+}{dy^+}\right) + \varphi_f + \mathrm{Re}_\tau \frac{d(\varphi_f \langle -u_f' v_f'\rangle^+)}{dy^+}\right]. \tag{24}$$

Since our particle volume fraction is low, we construct the drag formula without considering the hydrodynamic interactions between the particles. The force on one particle is

$$F_p = \frac{C_d}{2}\pi a^2 \rho_f |\langle u_f\rangle - \langle u_p\rangle|(\langle u_f\rangle - \langle u_p\rangle). \tag{25}$$

In Eq. (25), C_d represents the standard drag coefficient and is calculated with

$$C_d = \frac{24}{\mathrm{Re}_p}\left(1 + 0.15\mathrm{Re}_p^{0.687}\right), \tag{26}$$

where Re_p is the particle Reynolds number defined and computed by

$$\mathrm{Re}_p = \frac{2a|\langle u_f\rangle - \langle u_p\rangle|}{\nu} = \mathrm{Re}_\tau \frac{2a}{H}|\langle u_f\rangle^+ - \langle u_p\rangle^+|. \tag{27}$$

Then the dimensionless interphase force can be calculated from

$$\frac{F_x^+}{V^+} = \left(\frac{F_x}{V}\right)\frac{H}{\rho_f u_\tau^2} = \frac{\phi_s F_p}{\frac{4}{3}\pi a^3}\frac{H}{\rho_f u_\tau^2} = \frac{3\phi_s C_d |\langle u_f\rangle^+ - \langle u_p\rangle^+|(\langle u_f\rangle^+ - \langle u_p\rangle^+)}{8(a/H)}, \tag{28}$$

in which ϕ_s is the local solid volume fraction at a given y position, as shown in Fig. 7.

The interphase drag forces obtained from the balance theory [Eq. (24)] for $\rho_r = 1$, 10.42, and 104.2 are plotted in Fig. 10. The drag forces from the drag formula [Eq. (28)] for $\rho_r = 1$ and 104.2 are also plotted for comparison, and the case of $\rho_r = 10.42$ is not shown for the clarity of the figure. For $\rho_r = 104.2$, the balance theory and the drag formula predict the same behavior of the drag force: The drag on the particles is positive in the center region where the fluid average velocity is larger than the particle average velocity, and negative in the near-wall region where the particle average velocity is larger. Nevertheless, the drag formula underestimates the interphase force, which is understandable due to the following factors. First, the particle Reynolds number is not low so the drag force is not linearly proportional to the slip velocity. Therefore, the total drag obtained from the sum of the drags on the individual particles with different slip velocities is larger than that obtained with the average slip velocity. Second, the hydrodynamic interactions between the particles may increase the drag. Third, the particle finite-size effect, the wall effect, and the shear effect may affect the drag.

For $\rho_r = 1$, it is not surprising that the drag forces predicted from both methods are negative near the wall and almost vanish in the center region, since the particle average velocity is larger than the fluid average velocity near the wall and roughly equal to the fluid average velocity in the bulk region (see Fig. 5). However, it is interesting that the balance theory predicts a positive drag force on the particles in the region between

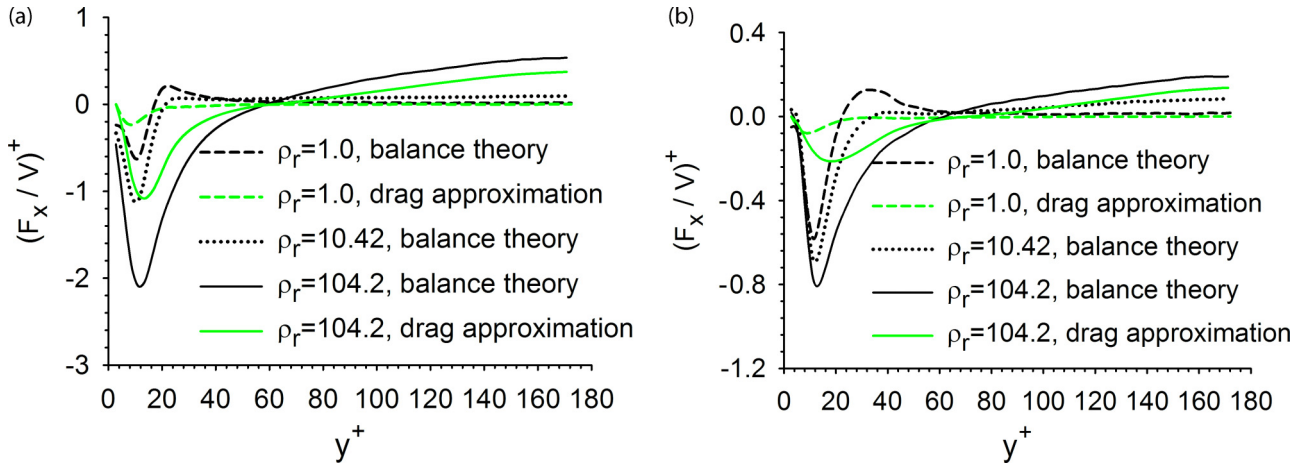

FIG. 10. The interphase forces obtained from the balance theory [Eq. (24)] and the drag formula [Eq. (28)] for (a) $a/H = 0.05$ and (b) $a/H = 0.1$. The red dash-dot lines represent zero force for reference.

the near-wall negative-force region and the center zero-force region, which cannot be predicted by the drag formula based on the interphase average slip velocity. From Eq. (23), the positive drag force is caused by the negative gradient of the particle total stress. Further, Fig. 9(b) shows that the particle inner stress is much larger than the particle Reynolds stress at $y^+ = 20-40$, and the decay of the particle inner stress with increasing y in this region is obviously responsible for the positive drag force on the particles.

The third equation for the fluid mean velocity is related to the pseudo body force (or Lagrange multiplier) λ introduced in the fictitious domain method for the rigid-body motion constraint on the fictitious fluids inside the particles [Eq. (A16)].

$$\mu\frac{d\overline{u}}{dy} + \int_0^y \overline{\lambda} d\xi + \rho_f(-\overline{u'v'}) = \tau_w\left(1 - \frac{y}{H}\right), \qquad (29)$$

where the overline represents the spatial averaging over a domain comprising both fluid and solid phases, i.e., $\overline{A} = \frac{1}{V}\int_V A dV$. The role of the pseudo body force is similar to the interphase force. Equation (A17) gives the relationship between them, which provides a simpler approach to compute the interphase force by using the pseudo body force than integrating the stress on the particle surface.

V. CONCLUSIONS

We have investigated the effects of finite-size particles with different density ratios on the turbulent channel flow by using a parallel direct-forcing fictitious domain method. The main findings are as follows:

(1) The variation of the flow drag with increasing particle-fluid density ratio is nonmonotonic and the flow drag is largest at the density ratio of the order of 10, as compared to the cases of the order of unity and 100. The drag reduction by the particles is observed during the transient stage for large particle density ratios, but not at the statistically stationary stage. It is not possible to judge whether the spherical particles can cause drag reduction for the fully developed turbulent flows without quantitative computations, since the presence of particles causes additional viscous dissipation which has dual effects on the friction drag of the turbulent flow: On the one hand, more viscous dissipation brings about directly larger flow drag, for the laminar flow case, while on the other hand, more viscous dissipation leads to suppression of the large-scale quasistreamwise vortices and thereby a lower flow resistance. Accurate simulations of the particle-fluid (turbulence) interactions with the improved discrete particle methods [44–46] or the interface-resolved direct simulations for small particles are required to confirm whether the significant drag reduction can be produced by the spherical particles.

(2) The particle fluctuation velocity generally decreases with increasing particle inertia, except that the particle streamwise fluctuation velocity and $\langle -u_p' v_p' \rangle$ in the near-wall region are largest when the particle density ratio is of the order of 10.

(3) Both particle collision and particle-turbulence interactions are responsible for the particle migration toward the channel center in a statistical sense for $a/H = 0.05$ and $\rho_r = 10.42$.

(4) The equations for the fluid mean velocity in terms of the solid stress and the interphase force are derived, respectively, from the spatial averaging theorem.

(5) The fluid Reynolds stress term decreases, while both particle Reynolds and inner stress terms increase, as the density ratio increases for the same particle size. The sum of the fluid Reynolds stress, the particle Reynolds stress and the particle inner stress terms does not change significantly with increasing density ratio, rendering the flow drag insensitive to the variation of the density ratio. The drag-reduction effect due to the decrease in the Reynolds shear stress is counteracted by the drag-enhancement effect due to the increase in the particle total stress or the interphase drag force, particularly for the case of large particle inertia. The contribution of the particle inner stress on the drag force is not sensitive to the density ratio, but is important for the nonmonotonic change of the drag coefficient.

(6) The interphase drag force obtained from the averaged momentum equation (the balance theory) agrees qualitatively with that from the empirical drag formula based on the phase-averaged slip velocity for large density ratios. For the neutrally buoyant case, the balance theory predicts a positive interphase

force on the particles arising from the negative gradient of the particle inner stress, which cannot be predicted by the drag formula based on the phase-averaged slip velocity. The drag formula based on the conditionally averaged slip velocity is a relevant subject for future study.

ACKNOWLEDGMENTS

The work was supported by the National Natural Science Foundation of China (Grants No. 11372275 and No. 11632016), and the Research Fund for the Doctoral Program of Higher Education of China (20130101110035). L.-P.W. is supported by the U.S. National Science Foundation (NSF) under CBET-1235974 and by the Air Force Office of Scientific Research under Grant No. FA9550-13-1-0213. Computing resources at Yellowstone supercomputer are provided by the National Center for Atmospheric Research through CISL-P35751014 and CISL-UDEL0001 and by the University of Delaware through NSF CRI 0958512.

APPENDIX

In this Appendix, we will derive the equations for the fluid mean velocity (or the flow drag) of the particle-laden turbulent channel flow under constant pressure gradient by using the spatial averaging theorem [50,51].

Suppose the volume V for averaging comprises the volume occupied by the fluid V_f and that by the particles V_p, and its surface, comprises the fluid part S_e^f and the solid part S_e^p, as shown in Fig. 11. The particle-fluid interface inside V is denoted by S_I. Note that the surface of V_f is $S_e^f + S_I$, whose outward unit normal is denoted by $\mathbf{n}_f$, and the surface of V_p is $S_e^p + S_I$, whose outward unit normal is denoted by $\mathbf{n}$. The spatial averaging of the fluid quantity A_f is defined by $\overline{A_f} = \frac{1}{V}\int_V A_f dV$ and its intrinsic phase average is defined by $\langle A_f \rangle = \frac{1}{V_f}\int_{V_f} A_f dV$. Clearly, $\overline{A_f} = \varphi_f \langle A_f \rangle$, φ_f being the local fluid volume fraction.

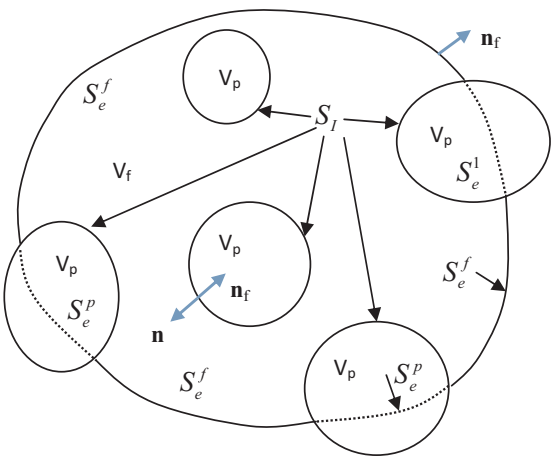

FIG. 11. Definitions of the volumes and interfaces for the spatial averaging.

The spatial averaging theorem states that [50]

$$\nabla \cdot \overline{A_f} = \frac{1}{V}\int_{S_e^f} A_f \cdot \mathbf{n}_f ds, \tag{A1}$$

which implies that the spatial derivative of an averaged quantity is related to the variation of this quantity on the surface of the volume.

From the spatial averaging theorem and the Guass theorem, one can obtain [50,51]

$$\overline{\nabla \cdot A_f} = \nabla \cdot \overline{A_f} - \frac{1}{V}\int_{S_I} A_f \cdot \mathbf{n} ds. \tag{A2}$$

In addition,

$$\overline{\frac{\partial A_f}{\partial t}} = \frac{\partial}{\partial t}\overline{A_f} + \frac{1}{V}\int_{S_I} A_f \mathbf{w} \cdot \mathbf{n} ds, \tag{A3}$$

where $\mathbf{w}$ is the velocity of the interface which is equal to the fluid velocity at the interface in the absence of the phase change.

The fluid momentum equation can be written as follows:

$$\frac{\partial(\rho_f \mathbf{u}_f)}{\partial t} + \nabla \cdot (\rho_f \mathbf{u}_f \mathbf{u}_f) = \nabla \cdot \sigma_f + \left(-\frac{dp_e}{dx}\right)\mathbf{e}_x, \tag{A4}$$

where ρ_f, u_f, σ_f, and $-\frac{dp_e}{dx}$ represent the fluid density, velocity, stress, and extra pressure gradient in the x-axis direction, respectively. Applying the spatial averaging theorem to (A4) yields

$$\frac{\partial(\varphi_f \rho_f \langle \mathbf{u}_f \rangle)}{\partial t} + \nabla \cdot (\varphi_f \rho_f \langle \mathbf{u}_f \mathbf{u}_f \rangle) = \nabla \cdot (\varphi_f \langle \sigma_f \rangle) + \varphi_f \left(-\frac{dp_e}{dx}\right)\mathbf{e}_x - \frac{1}{V}\int_{S_I} \mathbf{n} \cdot \sigma_f ds. \tag{A5}$$

For the channel flow at the statistically stationary state, Eq. (A5) for the x-axis direction is

$$\frac{d}{dy}(\varphi_f \langle \sigma_f \rangle_{xy}) + \varphi_f \left(-\frac{dp_e}{dx}\right) + \frac{d}{dy}(\varphi_f \rho_f \langle -u_f' v_f' \rangle) - \frac{F_x}{V} = 0, \tag{A6}$$

where u_f and v_f are the velocity components in the x and y directions, respectively, and $F_x = [\int_{S_I} \mathbf{n} \cdot \sigma_f ds]_x$, being the total interphase drag force on the particles in the band volume V (i.e., the volume between y and Δy for the case of channel flow). Note that the pressure term $\frac{d}{dx}(\varphi_f \langle p_f \rangle)$ [i.e., $\frac{d}{dx}(\varphi_f \langle \sigma_f \rangle_{xx})$ in (A5)] vanishes because p_f is periodic in the x-axis direction, and this term would exist and give identically the extra pressure gradient term in (A6) if the extra pressure gradient is not introduced in the momentum equation (A1) as the body force.

Since the solid momentum equation has the same form as the fluid one (A4), one can obtain the following solid counterpart of (A6):

$$\frac{d}{dy}(\varphi_s \langle \sigma_p \rangle_{xy}) + \varphi_s \left(-\frac{dp_e}{dx}\right) + \frac{d}{dy}(\varphi_s \rho_s \langle -u_p' v_p' \rangle) + \frac{F_x}{V} = 0, \tag{A7}$$

where the subscripts s and p denote the solid phase.

Adding (A6) to (A7) leads to

$$\frac{d}{dy}(\varphi_f\langle\sigma_f\rangle_{xy}+\varphi_s\langle\sigma_p\rangle_{xy})+\left(-\frac{dp_e}{dx}\right)+\frac{d}{dy}(\varphi_f\rho_f\langle-u_f'v_f'\rangle+\varphi_s\rho_s\langle-u_p'v_p'\rangle)=0. \quad \text{(A8)}$$

Equation (A8) is essentially the momentum equation for the fluid-solid mixture (i.e., suspension). $\varphi_f\langle\sigma_f\rangle_{xy}+\varphi_s\langle\sigma_p\rangle_{xy}$ is the shear stress of the suspension, and its value at the wall is the total wall stress τ_w. Integrating (A8) from the wall ($y=0$) to y and recalling that $-\frac{dp_e}{dx}=\frac{\tau_w}{H}$, one obtains

$$(\varphi_f\langle\sigma_f\rangle_{xy}+\varphi_s\langle\sigma_p\rangle_{xy})+(\varphi_f\rho_f\langle-u_f'v_f'\rangle+\varphi_s\rho_s\langle-u_p'v_p'\rangle)=\tau_w\left(1-\frac{y}{H}\right). \quad \text{(A9)}$$

The average fluid shear stress is related to the average fluid strain rate, which is

$$\overline{\nabla\mathbf{u}_f+(\nabla\mathbf{u}_f)^T}=\nabla(\varphi_f\langle\mathbf{u}_f\rangle)+[\nabla(\varphi_f\langle\mathbf{u}_f\rangle)]^T-\left[\frac{1}{V}\int_{S_I}(\mathbf{n}\mathbf{u}_f+\mathbf{u}_f\mathbf{n})ds\right]. \quad \text{(A10)}$$

From the spatial averaging theorem, $\nabla\varphi_f\approx\frac{1}{V}\int_{S_I}\mathbf{n}ds$; thus $(\nabla\varphi_f)\langle\mathbf{u}_f\rangle)+\langle\mathbf{u}_f\rangle\nabla\varphi_f\approx\frac{1}{V}\int_{S_I}(\mathbf{n}\langle\mathbf{u}_f\rangle+\langle\mathbf{u}_f\rangle\mathbf{n})ds$. Then (A10) reads

$$\overline{\nabla\mathbf{u}_f+(\nabla\mathbf{u}_f)^T}=\varphi_f\nabla\langle\mathbf{u}_f\rangle+\varphi_f(\nabla\langle\mathbf{u}_f\rangle)^T-\left[\frac{1}{V}\int_{S_I}(\mathbf{n}\mathbf{u}_\mathbf{f}'+\mathbf{u}_\mathbf{f}'\mathbf{n})ds\right]. \quad \text{(A11)}$$

The last term in (A11) is probably not important, considering that $\int_{\partial P}(\mathbf{n}\mathbf{u}_f+\mathbf{u}_f\mathbf{n})ds=0$ for the case of a rigid particle, here ∂P being the surface of any rigid particle. Therefore, this term is neglected here, and then

$$\varphi_f\langle\sigma_f\rangle_{xy}\approx\varphi_f\mu\frac{d\langle u_f\rangle}{dy}. \quad \text{(A12)}$$

Substituting (A12) into (A9), one obtains

$$\left(\varphi_f\mu\frac{d\langle u_f\rangle}{dy}+\varphi_s\langle\sigma_p\rangle_{xy}\right)+(\varphi_f\rho_f\langle-u_f'v_f'\rangle+\varphi_s\rho_s\langle-u_p'v_p'\rangle)=\tau_w\left(1-\frac{y}{H}\right). \quad \text{(A13)}$$

The momentum equation for our fictitious domain method is

$$\frac{\partial(\rho_f\mathbf{u})}{\partial t}+\nabla\cdot(\rho_f\mathbf{u}\mathbf{u})=-\nabla p+\mu\nabla^2\mathbf{u}+\boldsymbol{\lambda}+\left(-\frac{dp_e}{dx}\right)\mathbf{e}_x, \quad \text{(A14)}$$

and its corresponding averaged equation in the x-axis direction is

$$\frac{d}{dy}\left(\mu\frac{d\overline{u}}{dy}\right)+\left(-\frac{dp_e}{dx}\right)+\frac{d}{dy}(\rho_f\overline{-u'v'})+\overline{\lambda}=0. \quad \text{(A15)}$$

Integrating (A15) yields

$$\mu\frac{d\overline{u}}{dy}+\int_0^y\overline{\lambda}d\xi+\rho_f(-\overline{u'v'})=\tau_w\left(1-\frac{y}{H}\right). \quad \text{(A16)}$$

Because $\overline{u}=\varphi_f\langle u_f\rangle+\varphi_p\langle u_p\rangle$ and $\overline{-u'v'}=\varphi_f\langle-u_f'v_f'\rangle+\varphi_s\langle-u_p'v_p'\rangle$, from (A6), (A12), and (A15), we obtain

$$\frac{d}{dy}\left(\varphi_s\mu\frac{d\langle u_p\rangle}{dy}\right)+\varphi_s\left(-\frac{dp_e}{dx}\right)+\frac{d}{dy}(\varphi_s\rho_f\langle-u_p'v_p'\rangle)+\overline{\lambda}+\frac{F_x}{V}=0. \quad \text{(A17)}$$

Equation (A17) gives the relationship between the average pseudo body force and the average interphase drag force on the particles.

[1] K. D. Squires and J. K. Eaton, Particle response and turbulence modification in isotropic turbulence, Phys. Fluids A **2**, 1191 (1990).

[2] A. Ferrante and S. Elghobashi, On the physical mechanism of two-way coupling in particle-laden isotropic turbulence, Phys. Fluids **15**, 315 (2003).

[3] M. W. Vance, K. D. Squires, and O. Simonin, Properties of the particle velocity field in gas-solid turbulent channel flow, Phys. Fluids **18**, 063302 (2006).

[4] L.-P. Wang and M. R. Maxey, Settling velocity and concentration distribution of heavy particles in homogeneous isotropic turbulence, J. Fluid Mech. **256**, 27 (1993).

[5] S. Balachandar and J. K. Eaton, Turbulent dispersed multiphase flow, Annu. Rev. Fluid Mech. **42**, 111 (2010).

[6] A. Ten Cate, J. J. Derksen, L. M. Portela, and H. E. A. van den Akker, Fully resolved simulations of colliding monodisperse spheres in forced isotropic turbulence, J. Fluid Mech. **519**, 233 (2004).

[7] F. Lucci, A. Ferrante, and S. Elghobashi, Modulation of isotropic turbulence by particles of Taylor length-scale size, J. Fluid Mech. **650**, 5 (2010).

[8] H. Homann and J. Bec, Finite-size effects in the dynamics of neutrally buoyant particles in turbulent flow, J. Fluid Mech. **651**, 81 (2010).

[9] H. Gao, H. Li, and L.-P. Wang, Lattice Boltzmann simulation of turbulent flow laden with finite-size particles, Comput. Math. Appl. **65**, 194 (2013).

[10] M. Cisse, H. Homann, and J. Bec, Slipping motion of large neutrally buoyant particles in turbulence, J. Fluid Mech. **735**, R1 (2013).

[11] A. Chouippe and M. Uhlmann, Forcing homogeneous turbulence in direct numerical simulation of particulate flow with interface resolution and gravity, Phys. Fluids **27**, 123301 (2015).

[12] W. Fornari, F. Picano, G. Sardina, and L. Brandt, Reduced particle settling speed in turbulence, J. Fluid Mech. **808**, 153 (2016).

[13] J. C. B. de Motta, J. L. Estivalezes, E. Climent, and S. Vincent, Local dissipation properties and collision dynamics in a sustained homogeneous turbulent suspension composed of finite size particles, Int. J. Multiphase Flow **85**, 369 (2016).

[14] T. Wu, X. Shao, and Z. Yu, Fully resolved numerical simulation of turbulent pipe flows laden with large neutrally-buoyant particles, J. Hydrodyn. **23**, 21 (2011).
[15] T. Kajishima, S. Takiguchi, H. Hamasaki, and Y. Miyake, Turbulence structure of particle-laden flow in a vertical plane channel due to vortex shedding, JSME Int. J., Ser B **44**, 526 (2001).
[16] M. Uhlmann, Interface-resolved direct numerical simulation of vertical particulate channel flow in the turbulent regime, Phys. Fluids **20**, 053305 (2008).
[17] M. García-Villalba, A. G. Kidanemariam, and M. Uhlmann, DNS of vertical plane channel flow with finite-size particles: Voronoi analysis, acceleration statistics and particle-conditioned averaging, Int. J. Multiphase Flow **46**, 54 (2012).
[18] Y. Pan and S. Banerjee, Numerical investigation of the effects of large particles on wall turbulence, Phys. Fluids **9**, 3786 (1997).
[19] X. Shao, T. Wu, and Z. Yu, Fully resolved numerical simulation of particle-laden turbulent flow in a horizontal channel at a low Reynolds number, J. Fluid Mech. **693**, 319 (2012).
[20] A. G. Kidanemariam, C. Chan-Braun, T. Doychev, and M. Uhlmann, Direct numerical simulation of horizontal open channel flow with finite-size, heavy particles at low solid volume fraction, New J. Phys. **15**, 025031 (2013).
[21] M. Do-Quang, G. Amberg, G. Brethouwer, and A. V. Johansson, Simulation of finite-size fibers in turbulent channel flows, Phys. Rev. E **89**, 013006 (2014).
[22] F. Picano, W.-P. Breugem, and L. Brandt, Turbulent channel flow of dense suspensions of neutrally buoyant spheres, J. Fluid Mech. **764**, 463 (2015).
[23] L.-P. Wang, P. Gao, Z. Guo, and Z. Yu, Flow modulation by finite-size neutrally buoyant particles in a turbulent channel flow, J. Fluids Eng. **138**, 041306 (2016).
[24] W. Yu, I. Vinkovic, and M. Buffat, Acceleration statistics of finite-size particles in turbulent channel flow in the absence of gravity, Flow, Turbule. Combust. **96**, 183 (2016).
[25] W. Yu, I. Vinkovic, and M. Buffat, Finite-size particles in turbulent channel flow quadrant analysis and acceleration statistics, J. Turbul. **17**, 1048 (2016).
[26] P. Bagchi and S. Balachandar, Effect of turbulence on the drag and lift of a particle, Phys. Fluids **15**, 3496 (2003).
[27] T. M. Burton and J. K. Eaton, Fully resolved simulations of particle-turbulence interaction, J. Fluid Mech. **545**, 67 (2005).
[28] A. Naso and A. Prosperetti, The interaction between a solid particle and a turbulent flow, New J. Phys. **12**, 033040 (2010).
[29] V. Loisel, M. Abbas, O. Masbernat, and E. Climent, The effect of neutrally-buoyant finite-size particles on channel flows in the laminar-turbulent transition regime, Phys. Fluids **25**, 123304 (2013).
[30] I. Lashgari, F. Picano, W.-P. Breugem, and L. Brandt, Laminar, Turbulent, and Inertial Shear-Thickening Regimes in Channel Flow of Neutrally Buoyant Particle Suspensions, Phys. Rev. Lett. **113**, 254502 (2014).
[31] W. Fornari, A. Formenti, F. Picano, and L. Brandt, The effect of particle density in turbulent channel flow laden with finite size particles in semi-dilute conditions, Phys. Fluids **28**, 033301 (2016).
[32] Z. Yu, Z. Lin, X. Shao, and L.-P. Wang, A parallel fictitious domain method for the interface-resolved simulation of particle-laden flows and its application to the turbulent channel flow, Eng. Appl. Comput. Fluid Mech. **10**, 160 (2016).
[33] J. L. Lumley, Drag reduction by additives, Annu. Rev. Fluid Mech. **1**, 367 (1969).
[34] C. M. White and G. Mungal, Mechanics and prediction of turbulent drag reduction with polymer additives, Annu. Rev. Fluid Mech. **40**, 235 (2008).
[35] I. Radin, J. L. Zakin, and G. K. Patterson, Drag reduction in solid-fluid systems, AIChE J. **21**, 358 (1975).
[36] H. A. A. Bari and R. B. M. Yunus, Drag reduction improvement in two phase flow system using traces of SLES surfactant, Asian J. Ind. Eng. **1**, 1 (2009).
[37] L. H. Zhao, H. I. Andersson, and J. J. J. Gillissen, Turbulence modulation and drag reduction by spherical particles, Phys. Fluids **22**, 081702 (2010).
[38] R. Glowinski, T. W. Pan, T. I. Hesla, and D. D. Joseph, A distributed Lagrange multiplier/fictitious domain method for particulate flows, Int. J. Multiphase Flow **25**, 755 (1999).
[39] Z. Yu and X. Shao, A direct-forcing fictitious domain method for particulate flows, J. Comput. Phys. **227**, 292 (2007).
[40] T. Kempe and J. Fröhlich, Collision modelling for the interface-resolved simulation of spherical particles in viscous fluids, J. Fluid Mech. **709**, 445 (2012).
[41] J. C. B. de Motta, W.-P. Breugem, B. Gazanion, J.-L. Estivalezes, S. Vincent, and E. Climent, Numerical modelling of finite-size particle collisions in a viscous fluid, Phys. Fluids **25**, 083302 (2013).
[42] Z. Lin, X. Shao, Z. Yu, and L.-P. Wang, Effects of finite-size heavy particles on the turbulent flows in a square duct, J. Hydrodyn., Ser. B **29**, 272 (2017).
[43] J. K. Eaton, Two-way coupled turbulence simulations of gas-particle flows using point-particle tracking, Int. J. Multiphase Flow **35**, 792 (2009).
[44] M. R. Maxey and B. K. Patel, Localized force representations for particles sedimenting in Stokes flow, Int. J. Multiphase Flow **27**, 1603 (2001).
[45] J. Capecelatro and O. Desjardins, An Euler–Lagrange strategy for simulating particle-laden flows, J. Comput. Phys. **238**, 1 (2013).
[46] P. Gualtieri, F. Picano, G. Sardina, and C. M. Casciola, Exact regularized point particle method for multiphase flows in the two-way coupling regime, J. Fluid Mech. **773**, 520 (2015).
[47] M. W. Reeks, The transport of discrete particles in inhomogeneous turbulence, J. Aerosol Sci. **14**, 729 (1983).
[48] C. Marchioli and A. Soldati, Mechanisms for particle transfer and segregation in a turbulent boundary layer, J. Fluid Mech. **468**, 283 (2002).
[49] G. Sardina, P. Schlatter, L. Brandt, F. Picano, and C. M. Casciola, Wall accumulation and spatial localization in particle-laden wall flows, J. Fluid Mech. **699**, 50 (2012).
[50] S. Whitaker, *The Method of Volume Averaging* (Springer Science and Business Media, Berlin, 1999), Vol. 13.
[51] C. T. Crowe, J. D. Schwarzkopf, M. Sommerfeld, and Y. Tsuji, *Multiphase Flows with Droplets and Particles* (CRC Press, Boca Raton, FL, 2011).